TES Atmospheric Profile Retrieval Characterization: An Orbit of Simulated Observations

Susan Sund Kulawik, Helen Worden, Greg Osterman, Ming Luo, Reinhard Beer, Douglas E. Kinnison, Kevin W. Bowman, John Worden, Annmarie Eldering, Michael Lampel, Tilman Steck, and Clive D. Rodgers

***Abstract*—We test the accuracy of our error analysis and retrieval performance by examining retrievals over an orbits' worth of simulated data covering a variety of atmospheric conditions. The use of simulated data allows validation of the error analysis and retrieval algorithm by comparisons to the true values. To demonstrate typical results, two example retrievals are shown, along with associated diagnostic information. Curtain plots display comparisons between the retrieved results, the true values, and the initial guesses. The results show that the Tropospheric Emission Spectrometer (TES) retrieval algorithm is robust under a variety of atmospheric conditions, that TES can improve on the *a priori* for nadir species Tatim H_2O, O_3, and CO, and that the predicted errors match well with the actual retrieved errors. The target scenes (nadir, ocean, cloud-free) simulate conditions that are most easily validated with real data, and comparisons of on orbit results can be made with this baseline.**

***Index Terms*—EOS-Aura, error analysis, infrared spectroscopy, nonlinear estimation, simulation, Tropospheric Emission Spectrometer (TES).**

I. Introduction

THE Tropospheric Emission Spectrometer (TES) on the Earth Observing System Aura (EOS-Aura) platform measures thermal emission spectra of the Earth and atmosphere in both nadir and limb viewing modes. Using spectrally resolved emission/absorption features of atmospheric trace gases, the TES experiment can determine the vertical abundance profiles of several species that are key elements in atmospheric chemistry such as ozone, water vapor, carbon monoxide, and methane. For a more complete TES overview, see Beer *et al.* [1] and Beer [2]. This paper focuses on simulated TES nadir observations over ocean in clear-sky conditions in order to establish a reference for more complex cases. More complex cases include scenes with clouds and/or land scenes. For cloudy scenes, additional algorithms have been added to parameterize the cloud height and optical depths as a function of frequency. Kulawik *et al.* [3] discusses how clouds affect the trace gas retrieval error, sensitivity, and nonlinearity. Emissivity is also jointly retrieved in TES land scenes and is parameterized as a smoothly varying function of frequency. Propagation of emissivity errors into trace gas retrievals has been calculated and shown that these errors are small relative to the total error.

To demonstrate the algorithm results, examples of retrievals will be shown from simulated spectra generated using model atmospheric profiles sampled from the MOZART3 model [4], [5]. These retrieval examples are simulated measurements from a single TES orbit in order to test the algorithm response over a range of latitudes, temperatures, and atmospheric conditions. The MOZART3 vertical grid (on the order of 1 km) is finer than any feature retrieved by TES, and has sufficient vertical variability to test TES retrieval performance.

Use of simulated data allows validation of the retrieval algorithm and the assumptions of the error analysis. The validation of the error analysis is critical because this is the primary means of assessing the performance and consistency of retrievals with real data where the true state is not known. The error analysis quantities are statistical and are tested using an ensemble consisting of one orbit's worth of TES retrievals. The error analysis assumes Gaussian statistics and either linearity or moderate nonlinearity (as defined in [6]), and these assumptions are also tested.

Manuscript received April 22, 2005; revised December 5, 2005. This work was conducted by the Jet Propulsion Laboratory, California Institute of Technology, under a contract with the National Aeronautics and Space Administration.

S. S. Kulawik, H. Worden, G. Osterman, M. Luo, R. Beer, K. W. Bowman, J. Worden, and A. Eldering are with the Jet Propulsion Laboratory, Pasadena, CA 91109 USA (e-mail: Susan.Sund.Kulawik@jpl.nasa.gov).

D. E. Kinnison is with the National Center for Atmospheric Research, Boulder, CO 80301 USA.

M. Lampel is with Raytheon ITSS, Pasadena, CA 91101 USA.

T. Steck is with the Institut for Meteorologie und Klimaforschung, Forschungszentrum Karlsruhe, 76021 Karlsruhe, Germany.

C. D. Rodgers is with the Department of Physics, University of Oxford, Oxford OX1 3PU, U.K.

Digital Object Identifier 10.1109/TGRS.2006.871207

II. Single-Orbit Test Description

A. Simulated Observations

The simulated observations are created by determining the observation locations for one orbit, as described in Section II-A1, simulating the true state for each observation, as described in Section II-A2, and simulating the radiance from each true state, as described in Section II-A3.

1) Observation Locations: The ground track for one orbit is shown in Fig. 1. This ground track was specifically selected from the expected TES ground tracks in order to minimize land surface scenes. The Xs are about 5° apart along the orbit track, with observation 1 located nearest the South Pole.

2) True State Generation: The true atmosphere is taken from a MOZART3 [5] simulation driven with WACCM [7] meteorological fields for an October 2 day. The model atmosphere is representative of a present day distribution of chemical constituents. This MOZART3 dataset has 24 h of data with 20-min temporal and 2.8° spatial resolution. The 52 pressure levels range from 1000 to 0.1 hPa. The products used from MOZART3 were surface pressure, CH_4, H_2O, O_3, CO_2, CO,

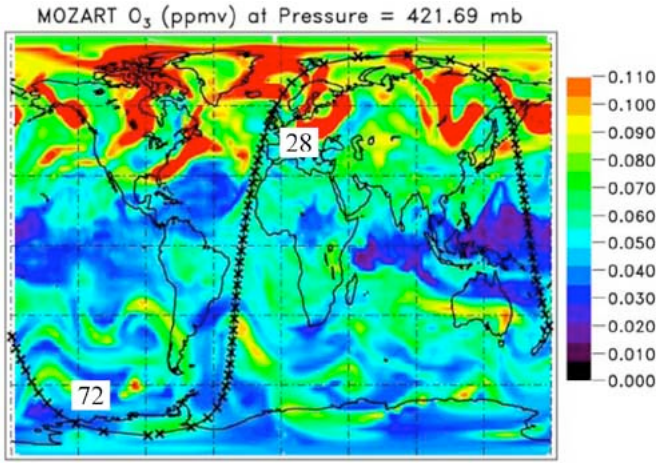

Fig. 1. MOZART3 model for O_3 at 422 hPa with TES nadir targets ($\mathbf{X}$'s) for a single orbit over-plotted. Observations 28 and 72 are labeled on this plot; the results at these locations are highlighted in Figs. 2 and 3.

NO_2, and T_{atm}. Surface temperature was set to the lowest T_{atm} level for both the initial guess and the true state (this will tend to underestimate TES sensitivity, especially in the boundary layer). The true state values were created from interpolation of the eight nearest dataset values (in latitude, longitude and time) of the MOZART3 dataset.

3) Simulated Spectra: The code to simulate the observed spectrum calculates the radiative transfer iteratively through an 86-layer atmosphere. The terms included in the radiative transfer calculation are upwelling atmospheric emission, downwelling, backreflected atmospheric emission, surface emission, and reflected sunlight. Following this calculation, which is on a frequency grid of 0.0004 to 0.0008 cm^{-1} (depending on the spectral region), the radiance is convolved with the TES instrument line shape, then apodized with Norton–Beer medium apodization [8] and sampled to a 0.06 cm^{-1} frequency grid. The absorption parameters used in the calculations were pre-calculated using a line-by-line code [9], [10] and the HITRAN spectroscopic database [11] which are calculated for every 10 K and for each of the 86 atmospheric layers. The TES forward model is described in more detail in Beer *et al.* [12] and Clough *et al.* [13].

B. Retrievals

To retrieve the nadir atmospheric state from TES data in a cloud-free scene with an ocean footprint, the following retrieval steps are performed sequentially: T_{atm}, H_2O, H_2O and T_{atm}, O_3, CH_4, and then CO. Surface temperature is also retrieved in all steps.

The initial individual temperature and water retrievals are initial guess refinements in preparation of a joint retrieval in step 3. T_{atm} and H_2O are retrieved first because they affect the retrieval of every other species.

1) Inversion: Each retrieval step iteratively minimizes a cost function using the Levenberg–Marquardt nonlinear least squares algorithm [14], where the cost function chosen considers both the spectroscopic fit over the spectral windows used (discussed in Section B5) and our *a priori* knowledge of the atmosphere. The cost function is

$$\text{Cost function} = \|\mathbf{L}_{\text{obs}} - \mathbf{L}(\mathbf{x},\mathbf{b})\|_{s_m} + \|\mathbf{z} - \mathbf{z}_c\|_{\Lambda}. \quad (1)$$

In the above equation, $\mathbf{L}_{\text{obs}}$ is the observed radiance (discussed in Section II-A3), $\mathbf{L}(\mathbf{x},\mathbf{b})$ is the radiance at the retrieved state and is calculated using the same radiative transfer code discussed in Section II-A3, S_m is the data noise error discussed in Section II-B2, x is the retrieved state (related to the retrieved quantities by a linear map), b represents nonretrieved parameters that affect the forward model, z are the retrieved quantities, z_c is the constraint vector (in our case set to the initial state), and A is the constraint matrix discussed in Section II-B3. Note that $\|A\|_B = ABA^T$. The retrieval is described in more detail in Bowman *et al.* [14].

2) Measurement NESR: The noise that is added to the simulated radiances in the single orbit test is estimated from the measured noise equivalent spectral radiance (NESR) from TES thermal vacuum calibration, described in [15]. Table I gives the bandpass frequency average of the modeled NESR expected for clear sky nadir views with a surface temperature around 300 K (this will tend to slightly overestimate polar noise) and for moderate Norton–Beer apodization (which reduces the NESR by a multiplicative factor of 0.665). These predicted NESR values are used as the standard deviation of Gaussian noise added to the simulated measurements after apodization, and the measurement covariance used for inversion and error estimation. For this exercise, the added noise for each spectral window is normalized to have zero mean and standard deviation exactly equal to predicted.

3) Constraints: Constraints were selected using the approach of Steck [16] and Kulawik [17], which select the constraint based on minimizing the expected error over an ensemble of retrievals, with the expected ensemble error described by (4).

Since T_{atm} and O_3 have information throughout the atmosphere, a first derivative exponential-decay Tikhonov constraint was used with a single strength parameter, described in [16]. The constraint strength was chosen using the initial guess Jacobians for each target scene using a cost function equal to the mean error between the surface and 10 hPa.

Since H_2O, CO, and CH_4 have less than one degree of freedom in parts of the atmosphere and/or throughout the atmosphere, altitude dependent zeroth and first derivative constraints were used for these species, with different weights of the zeroth and first derivative throughout the atmosphere, described in [17].

4) Initial State Generation: The initial guesses for all species except ozone were created through averaging of the true atmosphere. T_{atm} and H_2O, which are expected to have good initial guesses from metrology data, were created by averaging in a small region about the target scene location: all points within 2.8° latitude, 20° longitude, and 40 minutes. CH_4, N_2O, and CO initial guesses were created by averaging 20° latitude bins.

Ozone initial guesses were created from combinations of URAP[1] which covers pressures above 100 hPa and Harvard ozone profiles for 1992 [18] which cover from the surface to 10 hPa. For every latitude location, all profiles from September and October were found with 2° of that latitude and for all longitudes. If no profiles were found, the search latitude range was increased. When profiles were found, the URAP and Harvard profiles were separately averaged. Then the URAP and Harvard profile averages were smoothly combined into a single profile using log VMR/log Pressure interpolation.

The surface emissivity was set to sea water emissivity as measured by Masuda *et al.* [20] for both the initial states and the true states.

5) Spectral Windows Used in the SOT: The spectral windows are described in Worden [21]. These spectral windows were selected to maximize the information content of a retrieval given an expected *a priori* covariance from NCEP (for T_{atm} and H_2O) or MOZART3, data error, constraints, and atmospheric sensitivities.

C. Error Analysis Used in the SOT

This section provides a brief description of the error analysis, which includes measurement, smoothing, and interfering species error. For a more complete description, see Bowman *et al.* [14].

The error analysis assumes that we are in an incrementally linear regime, and that we could estimate our NLLS retrieved result with a linear equation which uses complete knowledge of the true state and radiance error vector [6], [21]:

$$\mathbf{x}_{\rm est} = \mathbf{x_a} + \mathbf{G}\varepsilon + \mathbf{A}(\mathbf{x}_{\rm true} - \mathbf{x_a}) + \mathbf{G}\mathbf{K_b}(\mathbf{b}_{\rm true} - \mathbf{b}_{\rm est}). \quad (2)$$

where is the averaging kernel, $\mathbf{x}_a$ is the *a priori* constraint vector, $\mathbf{x}_{\rm true}$ is the true state, $\mathbf{G}$ is the gain matrix, ε is the measurement error, $\mathbf{K}_b$ is the Jacobian matrix of the interfering species, and b is the state of the interfering species. $\mathbf{A}$ and $\mathbf{G}$ are calculated from the Jacobians of the retrieved species, the constraint matrix, and the estimated radiance errors.

The estimated error covariance matrix is defined as

$$S_{\rm err} = \langle(\mathbf{x}_{\rm est} - \mathbf{x}_{\rm true})(\mathbf{x}_{\rm est} - \mathbf{x}_{\rm true})^T\rangle. \quad (3)$$

This error covariance can be calculated using (2)

$$S_{\rm err} = \underbrace{(1-\mathbf{A})\mathbf{S}_a(1-\mathbf{A})^T}_{\rm smoothing} \underbrace{+\mathbf{G}\mathbf{S}_m\mathbf{G}^T}_{\rm measurement} + \underbrace{\mathbf{G}\mathbf{K_b}\mathbf{S}_{b\,\rm err}(\mathbf{G}\mathbf{K})^T}_{\rm systematic} \quad (4)$$

where $\mathbf{S}_a$ is the *a priori* covariance of the retrieved state, i.e., $\langle(\mathbf{X}_{\rm init} - \mathbf{X}_{\rm true})(\mathbf{X}_{\rm init} - \mathbf{X}_{\rm true})^T\rangle$, $\mathbf{S}_m$ is the measurement error covariance, and $\mathbf{S}_{\rm b}$ is the error covariance of the interfering species. The square-root diagonal of (4) gives the "error bars" commonly reported, and the various terms of (4) are helpful to determine the sizes of the various error components. Equation (4) is validated in the Results Section III-D.

[1]http://hvperion.gsfc.nasa.gov/Analversusis/UARS/ urap/home.html

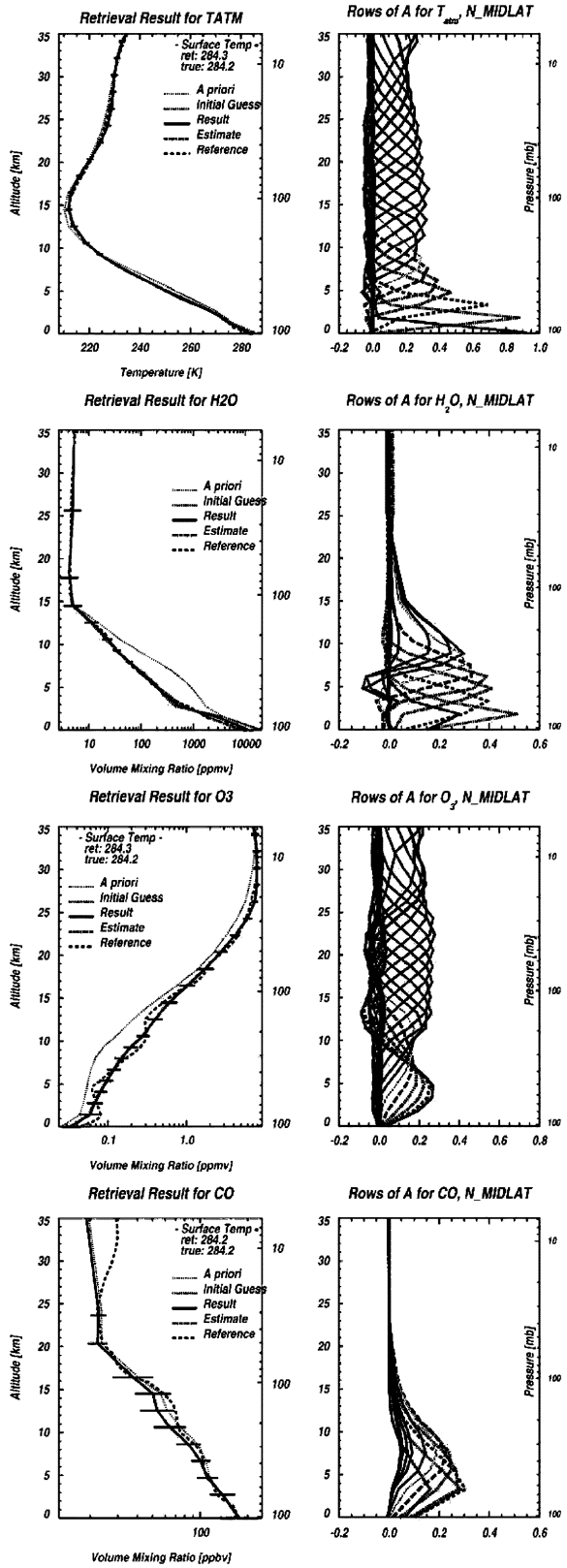

Fig. 2. Retrieval results for a north mid-latitude case (case 28).

D. A Priori Covariances

The *a priori* covariances are created by computing covariances with 1 days' worth of MOZART3 data, separated into five bins: North Polar (54 N to 90 N), North Midlat (18N to 54N), Tropics (18S to 18N), South Midlat (18S to 54S), and South

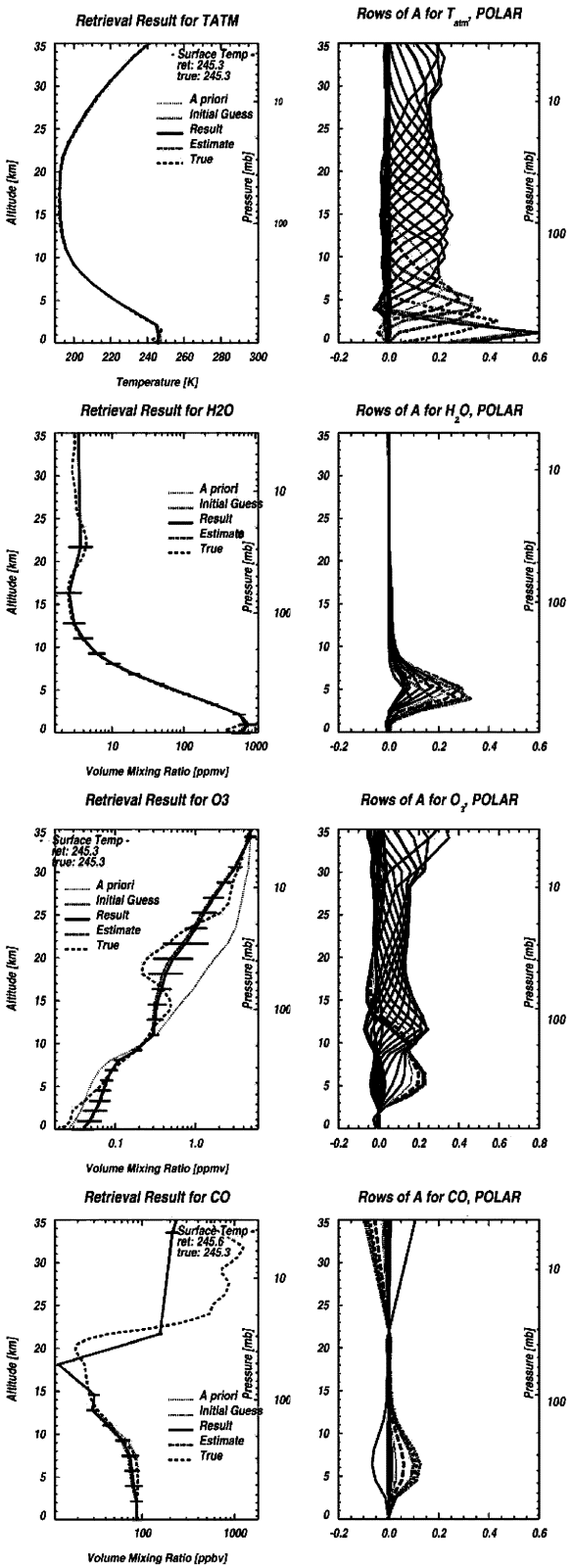

Fig. 3. Retrieval example for a polar target scene (case 72).

Polar (54S to 90S). The diagonal values for the covariance matrices of T_{atm} and H_2O are scaled to the NCEP uncertainty estimates,[2] which is the assumed uncertainty of the TES initial guess operationally.

[2]http://www.ncep.noaa.gov/.

TABLE I
BAND AVERAGE NESR VALUES USED FOR SIMULATED MEASUREMENTS AND RETRIEVALS

TES Filter ID	Frequencies (cm^{-1})	Nadir NESR, 16 pixel avg. ($nW/cm^2/sr/cm^{-1}$)
2B1	650-900	133
1B2	950-1150	17
2A1	1100-1325	17
1A1	1900-2250	23

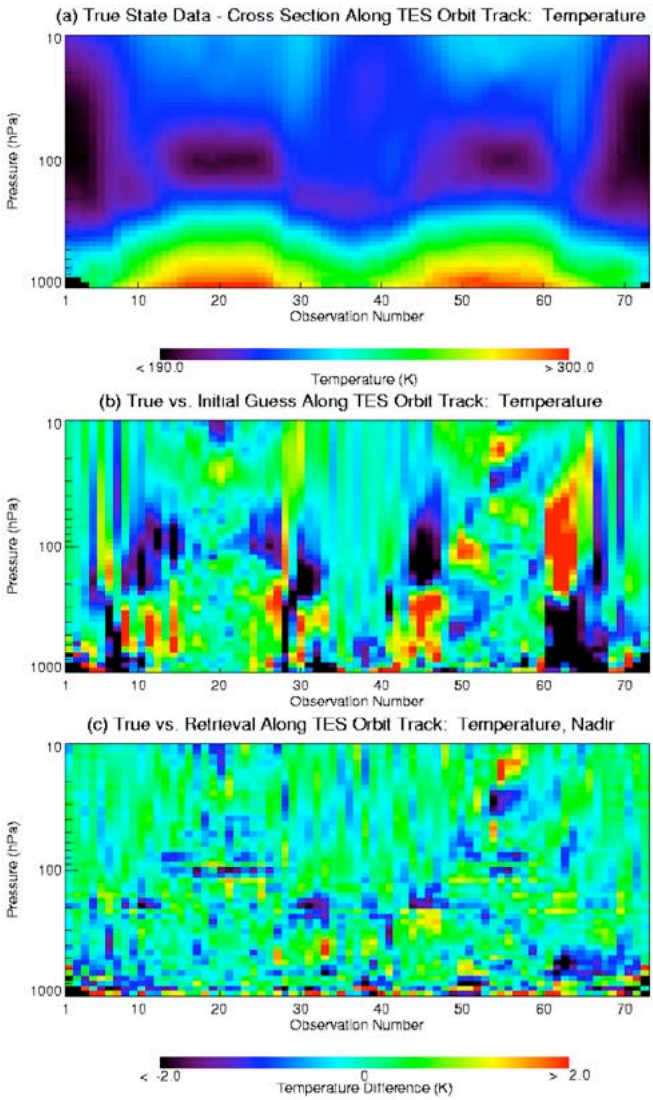

Fig. 4. (a) Temperature true states. (b) Initial error. (c) Retrieval error. (a) True stale data—cross section along TES orbit track: temperature. (b) True versus initial guess along TES orbit track: temperature. (c) True versus retrieval along TES orbit track: temperature, nadir.

III. RESULTS

A. Retrieval Example Plots With Corresponding Averaging Kernels

Figs. 2 and 3 show individual retrieval results for a North Midlatitude case (case 28) and a polar case (case 72). The left plots show the retrieval profile along with initial guess, *a priori*, true, and retrieval estimate [using (2)], which is usually directly over the result. The right plots show the rows of the averaging kernel which tell where the retrievals have sensitivity. The peak

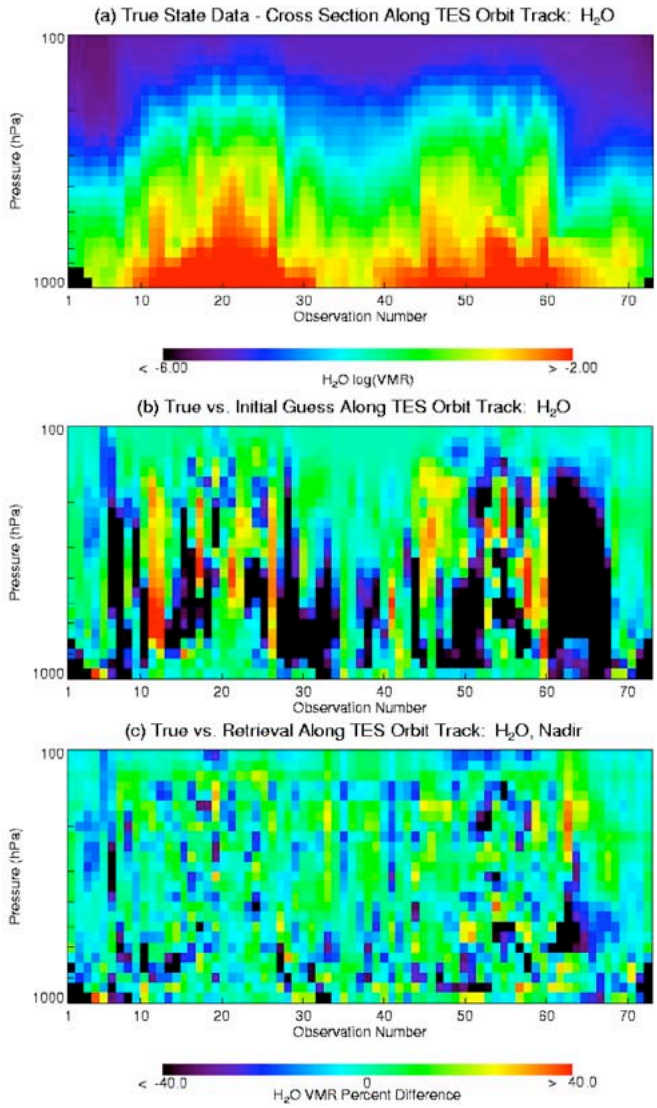

Fig. 5. (a) Water true states. (b) Initial error. (c) Retrieval error. (a) True state data—cross section along TES orbit track: H_2O. (b) True versus initial guess along TES orbit track: H_2O. (c) True versus retrieval along TES orbit track: H_2O Nadir.

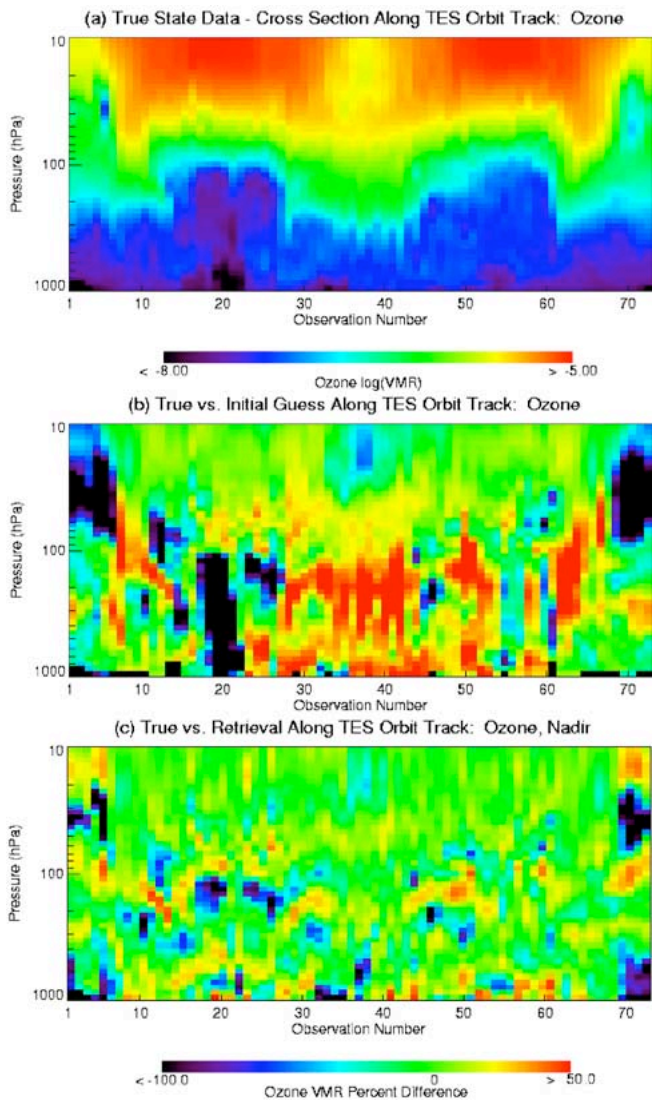

Fig. 6. (a) Ozone true states. (b) Initial error. (c) Retrieval error. (a) True state data—cross section along TES orbit track: ozone. (b) True versus initial guess along TES orbit track: ozone. (c) True versus retrieval along TES orbit track: ozone, nadir.

shows where the information for the retrieved state is coming from, the maximum tells what fraction of the retrieved value comes from the data versus the *a priori*, and the curve width shows the resolution. These are fairly representative results for most nonpolar and polar target scenes, respectively.

Although the temperature improvement appears modest in Fig. 2 due to the large dynamic range, it improves from about 3 K to about 1 K error. The averaging kernel shows that temperature information is retrieved throughout the entire atmosphere with the best resolution is between 0 and 5 km. The difference between *a priori* (light dotted) and initial guess (dark dotted) can be seen in the water retrieval, where the water refinement step did very well except at the surface. The refinement result was passed to the joint temperature/water retrieval which improves on this. The water averaging kernel shows that we have information from about 0 to 15 km with good resolution between about 0 and 8 km.

The ozone retrieval shows the capture of large-scale features but not the features less than 2 km. The averaging kernel shows the resolution (full width, half maximum) cannot capture 2 km features, as the resolution is about 8 km. The CO plot shows information coming from 3 to 12 km but with less total information than the other species. The retrieval shows a good match in this region.

Fig. 3 shows retrieval results for a South Pole case (case 72). T_{atm} and H_2O have an initial guess very close to true, however the O_3 displays some ozone depletion which was not expected by the initial guess. The retrieval captures the depletion, but does not fully resolve the features because the resolution is not fine enough (as seen in the averaging kernel plot). The polar plots show similar information patterns to midlatitude, but with somewhat less information overall. For example, water information is between 2 and 8 km rather than 0–15 km, and CO has information centered at about 6 km only.

TABLE II
RADIANCE RESIDUAL STATISTICS

	T_{atm} and H_2O	O_3	CO	CH_4
Radiance residual mean				
NMidlat	-0.007	0.000	-0.003	-0.099
Tropic	-0.002	-0.001	0.000	-0.021
SMidlat	-0.028	0.005	-0.002	-0.755
Polar	-0.010	-0.001	0.003	-0.239
Radiance residual r.m.s				
NMidlat	1.039	0.994	1.003	0.979
Tropic	1.019	1.019	0.997	1.009
SMidlat	1.047	0.985	1.010	0.959
Polar	1.028	1.008	0.992	0.946

TABLE III
PREDICTED VERSUS ACTUAL IMPROVEMENTS

	T_{atm}	H_2O	O_3	CO	CH_4
Mean error (Trop)					
Predicted:					
initial	1.6K	28%	42%	22%	2.0%
final	0.7K	15%	22%	19%	2.2%
Actual:					
Initial	1.3K	41%	45%	25%	2.5%
final	0.7K	15%	25%	19%	2.7%
Mean error (Strat)					
Predicted:					
initial	1.6K	31%	40%	12%	1.7%
final	0.7K	31%	18%	13%	1.6%
Actual:					
Initial	1.3K	1%	41%	52%	35.0%
final	0.7K	2%	20%	51%	34.4%
Column error					
Predicted:					
Initial	-	20.4%	2.1%	1.8%	1.7%
Final	-	1.2%	0.1%	1.1%	1.8%
Actual:					
initial	-	2.3%	2.0%	1.8%	0.04%
Final	-	0.9%	0.1%	1.5%	0.3%
Column error (trop)					
Predicted:					
Initial	-	20.4%	0.5%	1.8%	1.3%
Final	-	1.2%	0.8%	1.2%	1.4%
Actual:					
initial	-	2.3%	4.2%	1.9%	0.05%
Final	-	0.9%	1.6%	1.0%	0.25%

B. Curtain Plots of T_{atm}, H_2O, and O_3

Curtain plots are a way to show all target scene results in a few figures. Figs. 4–6 show results for T_{atm}, H_2O, and O_3 retrievals. The observation number is on the x axis and pressure is on the y axis with color representing the data value. The first plots [Figs. 4(a), 5(a), and 6(a)] show the variability of the true state for each target scene and pressure. T_{atm}, H_2O, and O_3 all show significant variability through the orbit. The second plots [Figs. 4(b), 5(b), and 6(b)] show the difference between the initial state and the true state. The third plots [Figs. 4(c), 5(c), and 6(c)] show the difference between the retrieved state and the true state. Figures (c) versus (b) show the extent of the improvement of the retrieved state over the initial state. T_{atm}, H_2O, and O_3 show significant improvement for the actual retrieved error over the actual initial error.

C. Data Residual Results

The radiance residual mean and covariance (normalized to the NESR) are important diagnostics. The residual mean is ideally zero and the covariance is ideally 1, and without the additional errors discussed below these should be exact, because the added noise was normalized to an ideal distribution. Deviations from this expectation are due to: 1) constraints in retrieved values due to mapping and retrieval constraints, fitting to noise, interfering species errors and 2) uncertainties resulting from instrument calibration, finite layer size, spectroscopy, and atmospheric inhomogeneity. List 1) are errors which could be encountered in this simulated test, and list 2) are errors which are encountered with real data only. The radiance residual mean and covariance are shown in Table II. The radiance residual mean results are reasonable except for CH_4 which seems to be fitting noise due to the small window size (0.66 cm^{-1}). The radiance residual covariance root-mean-square (rms) is close to 1.0 for O_3 and CO, and is 1.02–1.05 for the water/temperature step.

D. Error Analysis Validation

The TES error products, such as the final error covariance, allow results to be used properly, either for assimilation into global climate models, or to corroborate or refute particular theories or trends. This section validates the error analysis for the single orbit test by comparing predicted and actual errors.

Table III shows predicted and actual errors for some retrieved quantities. This table, in many cases, validates the error analysis for these averaged quantities. Note that the actual initial error is computed by taking the square root of the covariance *of (initial guess—true state)* for all targets. The actual final error is similarly computed by doing the same for the *(retrieval result—true state).* The predicted error is calculated using the same error analysis we use on orbit, and is validated by comparing to the actual error, a known quantity for simulated data.

The highlighted cases in Table III show cases where the actual and predicted initials errors agree relatively well. These cases show good agreement in the between the actual and predicted retrieval errors. The nonhighlighted cases show cases where the actual and predicted initials errors do not agree. However, these cases show the consistency that when the actual initial error is smaller than predicted, the actual retrieval error is smaller than predicted and vice versa. For example, *"Mean error (Strat)"* for H_2O predicts 31% error for both initial and final errors. However, the MOZART3 initial guess had only 1% error. It is not unexpected, given this information, that the final actual error is 2%, not 31%.

The error analysis is further examined using the predicted and actual errors in the retrieved profiles. The error analysis can be validated with the following three conditions:

1) *Error analysis is correct when all inputs are correct*
2) *Results are within a linear step of the true state*
3) *Inputs to the error analysis are correct*

Fig. 7 is used to validate the above three conditions. In Fig. 7, "- – –" shows the error analysis that is used for TES operational retrievals for each species averaged over this set of retrievals. "—" shows the assumed initial *a priori* errors. The red "—" and

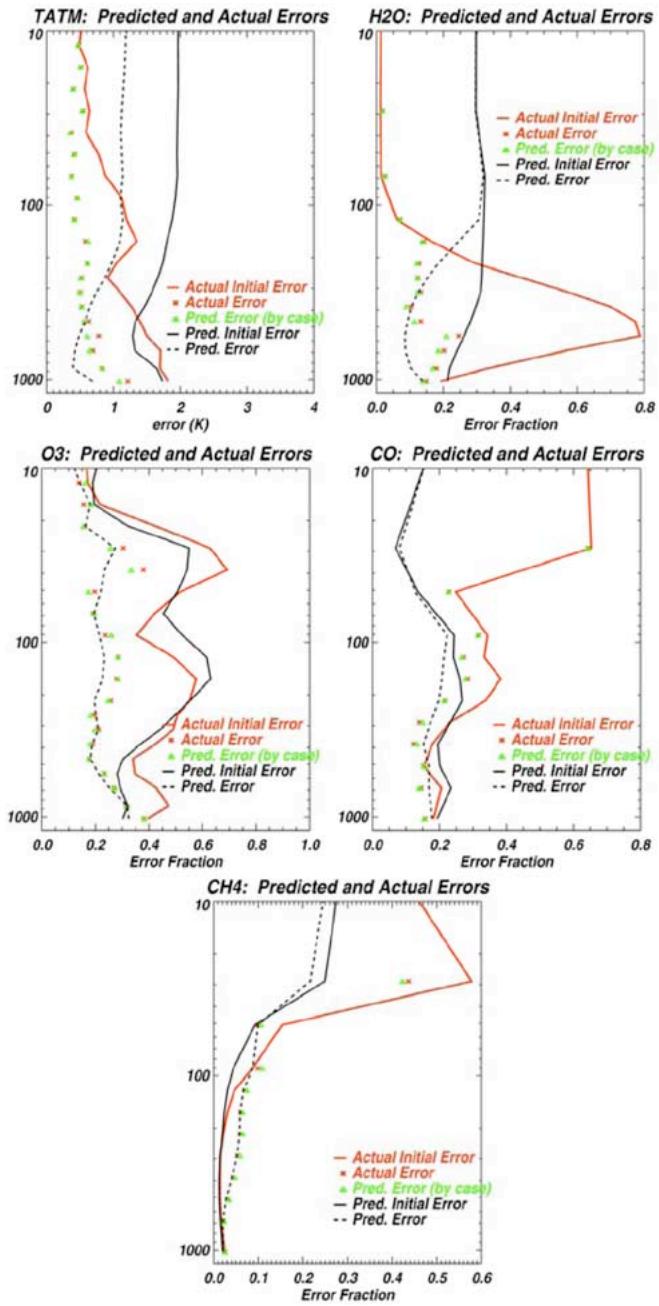

Fig. 7. Comparison of actual error $(x's)\sqrt{\langle(x_{\rm ret}-x_{\rm true})(x_{\rm ret}-x_{\rm true})^T\rangle_{ii}}$ versus - predicted error $(\Delta's)\sqrt{\langle(x_{\rm ret}-x_{\rm true})(x_{\rm ret}-x_{\rm true})^T\rangle_{ii}}$ where $\mathbf{x}_{\rm est}$ is calculated using (2). The agreement is quite good. The error bars (- - -) are in general different because the *actual* initial error (—)$(x's)\sqrt{\langle(x_{\rm init}-x_{\rm true})(x_{\rm init}-x_{\rm true})^T\rangle_{ii}}$ and the predicted initial error from climatology (—) $\sqrt{(S_a)_{ii}}$ differ.

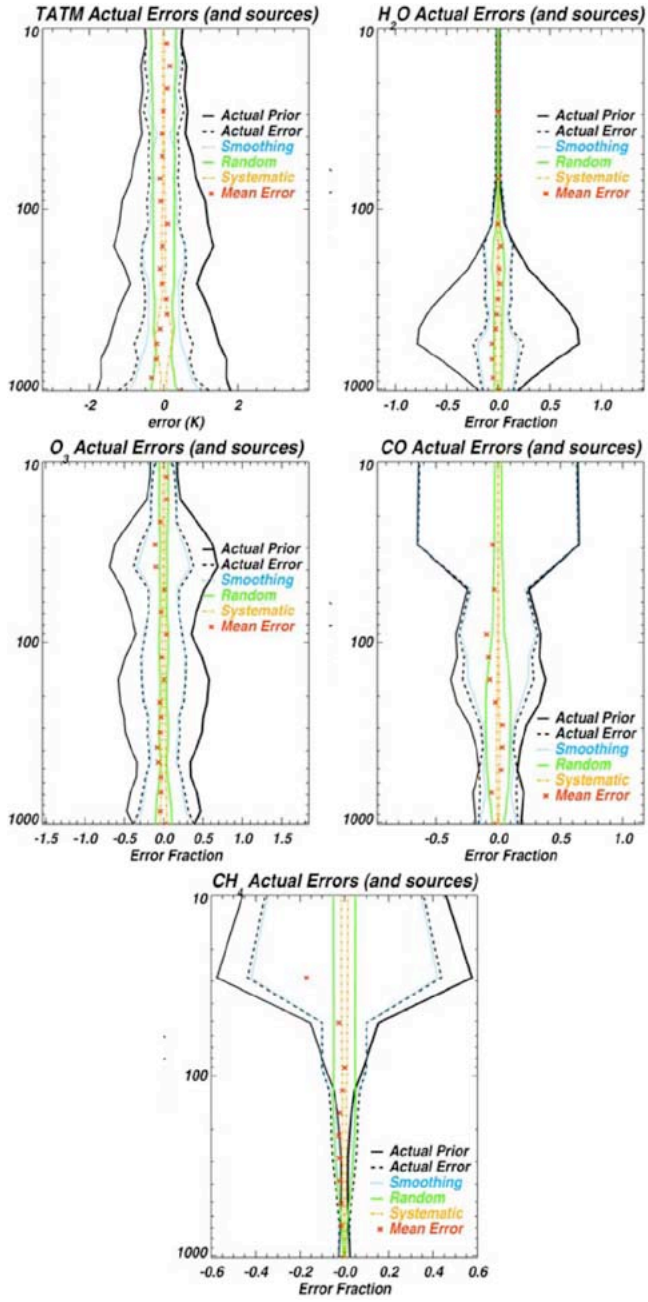

Fig. 8. Breakdown of actual errors, using (2), using true inputs from the single orbit test. These plots show that TES's dominant error is smoothing error [the second error term in (2)]. The black dashed line (- — —) shows the actual error and the x's show the mean error, $\langle\mathbf{x}_{\rm est}-\mathbf{x}_{\rm true}\rangle$.

"x" display the *actual* initial errors and retrieval errors, respectively. Finally, Δ shows the predicted errors using (2) using the Jacobians at the retrieved state and all other inputs set at their true values.

The agreement of x and Δ in Fig. 7 validates both conditions 1 and 2, since x is the actual error, and is from the linear error analysis (2) using the Jacobians at the retrieved state. The agreement, in general, is quite good, except for some minor under prediction in various places, and so conditions (1) and (2) are validated for the profile results of the atmospheric retrievals.

The agreement of x and - — —, the actual and predicted errors, respectively, would validate condition 3. This agreement in general is not as good. The disagreement occurs in locations where the initial predicted and actual errors (the black and red solids lines) do not agree. This highlights the dependency of the predicted errors on the *a priori* covariance through the smoothing error.

Fig. 8 shows the error breakdown into measurement error, smoothing error, and systematic error from interfering species.

This figure shows that in all cases, TES is dominated by smoothing error, which makes the predicted error highly dependent on our knowledge of the *a priori* covariance (note: the mean error is not subtracted out for the covariance calculation).

The *a priori* covariance for T_{atm} and H_2O is the MOZART3 covariance for 20 deg latitude bins scaled by the NCEP predicted errors, whereas the actual initial error is the true state minus a zonal average around the true state. Fig. 7 shows the discrepancy between the NCEP covariance and the actual initial error used for the SOT test. There is no expectation that these should match; the NCEP predictions were used for the predicted error because that is what we expect with real data. Inasmuch as these predictions are accurate, the TES error analysis with real data will be accurate because of the validation of TES error analysis when inputs are correct.

IV. Conclusion

The TES retrieval algorithm demonstrates robust retrievals over a wide range of atmospheric conditions as shown in Figs. 4–6. There is improvement, on average, over the initial guess for T_{atm}, H_2O, and O_3, and CO [Table II, and Figs. 4–6, panels (b) and (c)]. CH_4 will be addressed on orbit, when the spectroscopy can be assessed.

The sensitive regions where TES improves over the initial guess of the atmospheric state for TES nadir observations are as follows (see Fig. 7):

T_{atm}:	900–100 hPa
H_2O:	800–200 hPa
O_3:	700–20 hPa
CO:	400–200 hPa
CH_4:	40–90 hPa

The actual and predicted errors agree very well (within 2%) when inputs to the error analysis are accurate (Fig. 7 and Table III, highlighted portions). When the error analysis does not accurately predict the actual error, it was found to be because the initial error was smaller or larger than expected (Table III nonhighlighted portions, and Fig. 7), and because TES errors are dominated by smoothing errors (Fig. 7). This study highlights the importance of the initial atmospheric uncertainty on the accuracy of the TES reported retrieval errors.

It is important to note that for data assimilation or comparisons to models and other measurements, such as sondes, the smoothing error can be explicitly removed from the comparison by substituting the measurement or model profile for the true state in (2), [22], and [23]. The simulated results show that the errors, after accounting for smoothing, are accurate under a variety of atmospheric conditions.

Acknowledgment

The authors would like to thank J. Logan, T. Clough, M. Shepherd, the TES science team, and the TES software team.

References

[1] R. Beer, T. Glavich, and D. Rider, "Tropospheric Emission Spectrometer for the Earth Observing System's Aura satellite," *Appl. Opt.*, vol. 40, pp. 2356–2367, 2001.

[2] R. Beer, "TES on the Aura mission: Scientific objectives, measurements, and analysis overview," *IEEE Trans. Geosci. Remote Sens.*, vol. 44, no. 5, pp. 1102–1105, May 2006.

[3] S. S. Kulawik, J. Worden, A. Eldering, K. W. Bowman, M. Gunson, G. Osterman, L. Zhang, D. Jacob, S. A. Clough, M. Shephard, and R. Beer, "Implementation of cloud retrievals for Tropospheric Emission Spectrometer (TES) atmospheric observations—Part I: Description and characterization of errors on trace gas estimates," *J. Geophys. Res.—Atmos.*, 2006, to be published.

[4] G. P. Brasseur, D. A. Hauglustaine, S. Walters, P. J. Rasch, J. F. Muller, C. Granier, and X. X. Tie, "MOZART: A global chemical transport model for ozone and related chemical tracers 1: Model description," *J. Geophys. Res.—Atmos.*, vol. 103, pp. 28 265–28 289, 1998.

[5] M. Park, W. J. Randel, D. E. Kinnison, R. R. Garcia, and W. Choi, "Seasonal variation of methane, water vapor, and nitrogen oxides near the tropopause: Satellite observations and model simulations," *J. Geophys. Res.—Atmos.*, vol. 109, no. D3, 2004.

[6] C. D. Rodgers, *Inverse Methods for Atmospheric Sounding: Theory and Practice*, Singapore: World Scientific, 2000.

[7] F. Sassi, D. Kinnison, B. A. Boville, R. R. Garcia, and R. Roble, "Effect of El Nino-Southern OPscillation on the dynamical, thermal, and chemical structure of the middle atmosphere," *J. Geophys. Res.—Atmos.*, vol. 109, no. D17, 2004.

[8] R. H. Norton and R. Beer, "New apodizing functions for Fourier spectrometry," *J. Opt. Soc. Amer.*, vol. 66, no. 3, pp. 259–264, 1976.

[9] S. A. Clough and M. J. Lacono, "Line-by-line calculations of atmospheric fluxes and cooling rates II: Application to carbon dioxide, ozone, methane, nitrous oxide, and the halocarbons," *J. Geophys. Res.*, vol. 100, pp. 16 519–16 535, 1995.

[10] S. A. Clough, M. J. lacono, and J.-L. Moncet, "Line-by-line calculation of atmospheric fluxes and cooling rates: Application to water vapor," *J. Geophys. Res.*, vol. 97, pp. 15 761–15 785, 1992.

[11] L. S. Rothman, C. P. Rinsland, A. Goldman, S. T. Massie, D. P. Edwards, J. M. Flaud, A. Perrin, C. Camy-Peyret, V. Dana, J. Y. Mandin, J. Schroeder, A. McCann, R. R. Gamache, R. B. Wattson, K. Yoshino, K. V. Chance, K. W. Jucks, L. R. Brown, V. Nemtchinov, and P. Varanasi, "The HITRAN molecular spectroscopic database and HAWKS (HITRAN Atmospheric Workstation): 1996 edition," *J. Quant. Spectrosc. Radiat. Transf.*, vol. 60, pp. 665–710, 1998.

[12] R. Beer, K. W. Bowman, P. D. Brown, S. A. Clough, A. Goldman, D. J. Jacob, J. A. Logan, M. Luo, F. J. Murcray, D. M. Rider, C. P. Rinsland, C. D. Rodgers, E. A. Ustinov, H. M. Worden, and M. Syvertson, Eds., "Tropospheric Emission Spectrometer (TES) Level 2 Algorithm Theoretical Basis Document, V. 1.1," JPL, Pasadena, CA, JPL D-16474, Oct. 1999. [Online]. Available: http://eospso.gsfc.nasa.gov/atbd/testables.html.

[13] S. A. Clough, M. W. Shephard, J. Worden, P. O. Brown, H. Worden, M. Luo, C. D. Rodgers, C. P. Rinsland, A. Goldman, L. Brown, S. S. Kulawik, A. Eldering, M. C. Lampel, G. Osterman, R. Beer, K. Bowman, K. E. Cady-Pereira, and E. J. Mlawer, "Forward model and Jacobians for Tropospheric Emission Spectrometer retrievals," *IEEE Trans. Geosci. Remote Sens.*, vol. 44, no. 5, pp. 1308–1323, May 2006.

[14] K. W. Bowman, C. D. Rodgers, S. S. Kulawik, J. Worden, E. Sarkissian, G. Osterman, T. Steck, M. Lou, A. Eldering, M. Shephard, H. Worden, M. Lampel, S. Clough, P. Brown, C. Rinsland, M. Gunson, and R. Beer, "Tropospheric Emission Spectrometer: Retrieval method and error analysis," *IEEE Trans. Geosci. Remote Sens.*, vol. 44, no. 5, pp. 1297–1307, May 2006.

[15] H. Worden, R. Beer, K. Bowman, B. Fisher, M. Luo, D. Rider, E. Sarkissian, D. Tremblay, and J. Zong, "TES level l algorithms: Interferogram processing, geolocation, radiometric, and spectral calibration," *IEEE Trans. Geosci. Remote Sens.*, vol. 44, no. 5, pp. 1288–1296, May 2006.

[16] T. Steck, "Methods for determining regularization for atmospheric retrieval problems," *Appl. Opt.*, vol. 41, pp. 1788–1797, Mar. 20, 2002.

[17] S. S. Kulawik, G. Osterman, and D. Jones, "Calculation of altitude-dependent Tikhonov constraints for TES nadir retrievals," *IEEE Trans. Geosci. Remote Sens.*, vol. 44, no. 5, pp. 1334–1342, May 2006.

[18] J. A. Logan, "An analysis of ozonesonde data for the troposphere: Recommendations for testing 3-D models, and development of a gridded climatology for tropospheric ozone," *J. Geophys. Res.*, vol. 104, pp. 16 115–16 149, 1999.

[19] J. A. Logan, "An analysis of ozonesonde data for the lower stratosphere: Recommendations for testing models," *J. Geophys. Res.*, vol. 104, pp. 16 151–16 170, 1999.
[20] K. Masuda, T. Takashima, and Y. Takayama, "Emissivity of pure and sea waters for the model sea surfaces in the infrared window regions," *Remote Sens. Environ.*, vol. 24, pp. 313–329, 1988.
[21] J. Worden, S. S. Kulawik, M. W. Shephard, S. A. Clough, H. Worden, K. Bowman, and A. Goldman, "Predicted errors of Tropospheric Emission Spectrometer nadir retrievals from spectral window selection," *J. Geophys. Res.—Atmos.*, vol. 109, no. D9, 2004. DOI: 10.1029/2004JD004522.
[22] C. D. Rodgers and B. J. Connor, "Intercomparison of remote sounding instruments," *J. Geophys. Res.—Atmos.*, vol. 108, no. D3, 2003. DOI: 10.1029/2002JD002299.
[23] D. B. A. Jones, K. W. Bowman, P. I. Palmer, J. R. Worden, D. J. Jacob, R. N. Hoffman, I. Bey, and R. M. Yantosca, "Potential of observations from the Tropospheric Emission Spectrometer to constrain continental sources of carbon monoxide," *J. Geophys. Res.—Atmos.*, vol. 108, no. D24, 2003.

Susan Sund Kulawik received the B.S. degree from The Ohio State University, Columbus, in 1991 and the Ph.D. in physics from the University of Michigan, Ann Arbor, in 1999.

She is a member of the Tropospheric Emission Spectrometer (TES) Science Team and has worked on TES since 1999, first at Raytheon ITSS in Pasadena, CA, and at the Jet Propulsion Laboratory, Pasadena, since 2002. Her research interests include the use of information theory to select constraints and spectral windows, error analysis, retrievals in the presence of clouds, and HNO_3 retrievals from TES data.

Helen Worden received the Ph.D. degree in particle physics from Cornell University, Ithaca, NY, in 1991.

She and has worked at the Jet Propulsion Laboratory since 1993, where she is a member of the Tropospheric Emission Spectrometer (TES) Science Team and works on calibration and retrieval algorithms.

Gregory Osterman received the B.S. degree in physics from Texas A&M University, College Station, in 1987, the M.S. degree in physics from Texas Tech University, Austin, and the Ph.D. degree in physics from the University of Texas at Dallas, Richardson, in 1994.

He is a member of the Tropospheric Emission Spectrometer (TES) Science Team, Jet Propulsion Laboratory, Pasadena, CA, and focuses primarily on validation of TES data. His research interests also include studying tropospheric ozone using TES and other data sources as well as models.

Ming Luo received the Ph.D. degree in atmosphere and space sciences from the University of Michigan, Ann Arbor, in 1991.

She is a member of the Tropospheric Emission Spectrometer (TES) Science Team, Jet Propulsion Laboratory, Pasadena, CA, and works on L2 forward model and retrieval algorithms, data calibration and validation, and L3 algorithms including visualization of TES data.

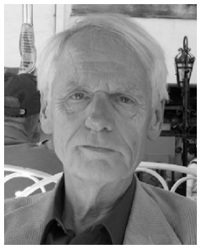

Reinhard Beer received the Ph.D. degree in physics from the University of Manchester, Manchester, U.K., in 1960.

He joined the Jet Propulsion Laboratory, Pasadena, CA, in 1963, where he is the Principal Investigator for the Tropospheric Emission Spectrometer on the Earth Observing System Aura satellite launched on July 15, 2004.

Douglas E. Kinnison received the Ph.D. degree in physical chemistry from the University of California at Berkeley.

He is currently a Project Scientist at the National Center for Atmospheric Research (NCAR), Boulder, CO. His research specialties include atmospheric chemistry and modeling of global atmospheric processes. He is currently responsible for the implementation and evaluation of the chemistry component of the Whole Atmosphere Community Climate Model (WACCM) and the Model for OZone And Related chemical Tracers, Version 3 (MOZART3). He is also a co-investigator on the EOS Aura High Resolution Dynamical Limb Sounder (HIRDLS) instrument.

Kevin W. Bowman received the B.E.E. degree in electrical engineering from Auburn University, Auburn, AL, the Diplome de Specialization en Traitement et Transmission des Informations from the Ecole Superieure d'Electricite (SUPELEC), Metz, France, the M.S. and Ph.D. in electrical engineering at the Georgia Institute of Technology, Atlanta, in 1991, 1992, 1993, and 1997, respectively.

He has been a Member of the Technical Staff at the Jet Propulsion Laboratory, Pasadena, CA, since 1997. His primary research interests are in the area of atmospheric remote sensing and tropospheric chemistry including inverse modeling and data assimilation from satellite observations, estimation and error analysis of trace gas profiles, and calibration algorithms for infrared Fourier transform spectrometers.

John Worden received the B.S. degree in physics from the University of California at Santa Cruz in 1990 and the Ph.D. degree in physics from the University of Colorado, Boulder, in 1996.

He has worked on the Tropospheric Emission Spectrometer (TES) since 1999, as a member of the TES science team at the Jet Propulsion Laboratory, Pasadena, CA (since 2002), at Raytheon ITSS, Pasadena (2000–2002), and at Atmospheric and Environmental Research, Cambridge, MA (1999–2000). His research interests include retrievals of atmospheric composition, radiative transfer through the atmosphere, understanding the water cycle using measurements of water and its isotopes, and atmospheric pollution sources and sinks.

Annmarie Eldering received the B.E. degree in chemical engineering from Cooper Union, New York, in 1988 and the Ph.D. degree in environmental engineering from the California Institute of Technology, Pasadena, CA, in 1994.

She is a Research Scientist at the Jet Propulsion Laboratory, Pasadena. Her research interests include cloud characterization from remote sensing measurements of clouds and the impact of clouds and water vapor on climate.

Michael Lampel received the B.A. degree in physics from the College of Creative Studies, University of California at Santa Barbara in 1976, and the M.A. and Ph.D. degrees in physics from the University of California, Berkeley, in 1978 and 1984, respectively.

He is the Science Lead for Raytheon Information Solutions Science Systems and Analysis Department, Pasadena, CA, and has worked on the Tropospheric Emission Spectrometer (TES) since 1998. His primary work has been in applied physics and modeling: medical imaging, free electron lasers, particle beams, radiative transfer, and atmospheric remote sensing.

Tilman Steck received the Diploma in physics from the University of Tübingen, Tübingen, Germany, in 1996 and the Ph.D. degree in physics from the University of Karlsruhe (TH), Karlsruhe, Germany, in 2000.

He has worked in the area of atmospheric remote sensing since 1996, especially in the development of retrieval algorithms and selection of constraints for the Michelson Interferometer for Passive Atmospheric Sounding (MIPAS) on Envisat. He held a postdoctoral position at the California Institute of Technology, Pasadena, at the Jet Propulsion Laboratory during 2000 and 2001, in the TES Science Team. He is currently working at the Institute for Meterological and Climate Research, which is jointly operated at the University of Karlsruhe and the Karlsruhe Research Centre, as a member of the MIPAS satellite group.

Clive D. Rodgers received the B.A., M.A., and Ph.D. in physics from Cambridge University, Cambridge, U.K., in 1960, 1963, and 1964, respectively.

He was a University Lecturer in the Department of Physics at the University of Oxford from 1967 until his retirement in 2001. He has continued his research as a Senior Research Fellow at Jesus College, University of Oxford. His main research interests include radiative transfer, molecular spectroscopy, the application of estimation theory to the inverse problem of radiative transfer, and the application and assimilation of satellite data to stratospheric and mesospheric dynamics and chemistry. He is the author of *Inverse Methods for Atmospheric Sounding: Theory and Practice* (World Scientific, 2001).